Biophysical Journal, Volume *117*

Supplemental Information

Multiscale Modeling of Dyadic Structure-Function Relation in Ventricular Cardiac Myocytes

Filippo G. Cosi, Wolfgang Giese, Wilhelm Neubert, Stefan Luther, Nagaiah Chamakuri, Ulrich Parlitz, and Martin Falcke

Supplementary Material
Multi-scale modeling of dyadic structure-function relation in ventricular cardiac myocytes

Filippo G. Cosi, Wolfgang Giese, Wilhelm Neubert,
Stefan Luther, Nagaiah Chamakuri, Ulrich Parlitz, Martin Falcke*

*corresponding author: martin.falcke@mdc-berlin.de

Contents

1 Supplementary Text

Mathematical model

The mathematical model comprises several scales ranging from single receptors and ion channels to whole cell electrophysiology. The cell volume is described by a domain $\Omega \subset \mathbb{R}^3$ and the plasma membrane, meaning its boundary, by Γ. The dynamics of the cytosolic Ca^{2+} concentration, c, comprise plasma membrane transport, release and uptake by the SR and binding to buffers. Plasma membrane transport is carried by the voltage controlled ion channels and the NCX. The T-tubule network is an interface to the extracellular fluid in the bulk of the cytosol enabling membrane molecules like the NCX to contribute to bulk concentration dynamics (J_{NaCa}, see Eq (S1)). The term J_{pump} describes the pumping of Ca^{2+} by SERCAs into the SR. The Ca^{2+}-binding molecules ($b_j, j = s, m, f$) in the cytosol include stationary (s), mobile (m) and fluorescent (f) Ca^{2+} buffers. The total concentration b^j_{tot} is conserved for each of the buffers. The reaction terms $R_j(c, b_j)$ describe buffering in the dynamics of cytosolic Ca^{2+}. The partial differential equations for the cytosolic species are

$$\frac{\partial c}{\partial t} = \nabla \cdot (\mathbf{D}_c \nabla c) + J_{\mathrm{cru}} + J^{\mathrm{vol}}_{\mathrm{NCX}} + J_{\mathrm{leak}} - J_{\mathrm{pump}} - \sum_{j=m,s,f} R_j(c, b_j) \quad \text{in } \Omega \times [0, T], \tag{S1}$$

$$\frac{\partial b_j}{\partial t} = \nabla \cdot (\mathbf{D}^j_b \nabla b_j) + R_j(c, b_j), \qquad j = s, m, f \quad \text{in } \Omega \times [0, T], \tag{S2}$$

where $\mathbf{D}$ and $\mathbf{D}^j_b$ are diagonal diffusion matrices. In the current implementation, isotropic diffusion is assumed. The expressions for the fluxes are

$$J_{\mathrm{cru}} = \sum_{i=1}^{N_{\mathrm{cru}}} \Theta(R^i_{\mathrm{cru}} - |\mathbf{r} - \mathbf{r}_i|) J^i_c(c, V_m, t), \tag{S3}$$

$$J_{\mathrm{leak}} = V_l(c_{\mathrm{sr}} - c), \tag{S4}$$

$$J_{\mathrm{pump}} = V^{\max}_p \frac{c}{K_p + c} \frac{c_{\mathrm{sr},0}}{c_{\mathrm{sr}}}, \tag{S5}$$

$$R_j(c, b_s, \mathbf{r}) = k^+_j (b^{\mathrm{tot}}_m - b_m)c - k^-_m b_m, \tag{S6}$$

where $\Theta(x)$ is the Heaviside step function, k_j^+ and k_j^- are the binding and dissociation rates for the buffer j (for $j = m, s, f$). Ca^{2+} influx through LCC (I_{LCC}) and release through RyR (I_{RyR}) channels occur mainly in dyadic clefts (J_{cru}). The dependence on time of J_{cru} is caused by their stochastic behavior.

The space inside CRUs is described as a flat cylinder in the detailed CRU model. The interface between dyadic space and cytosol through which Ca^{2+} leaves the CRU is a band twisted in 3 dimensions since the jSR wraps around T-tubules. Since we cannot represent the shape of this interface for each CRU on the level of the PDEs, its geometry is approximated as spherical source volume centered at $\mathbf{r}_i$ with radius R^i_{cru} and random flux $J^i_c(c(\mathbf{r}_i), V_m, t)$. The flux $J^i_c(c, V_m, t)$ is the sum of all single channel LCC- and RyR-currents in the ith CRU divided by $\frac{4}{3}\pi \left(R^i_{\mathrm{cru}}\right)^3$.

The boundary conditions for the above PDEs are given by the plasma membrane Ca^{2+}-currents

$$\mathbf{n} \cdot \mathbf{D}_c \nabla c = J^{pm}_{\mathrm{NCX}} \text{ on } \Gamma \times [0, T], \tag{S7}$$

$$\mathbf{n} \cdot \mathbf{D}_{b_j} \nabla b_j = 0 \text{ on } \Gamma \times [0, T], \tag{S8}$$

where J^{pm}_{NCX} is the plasma membrane part of the NCX flux. Ca^{2+} is released into dyadic clefts from specialized parts of the sarcoplasmic reticulum called junctional sarcoplasmic reticulum (jSR). The jSR of the individual CRUs are coupled to the network SR by a diffusional flux

$$J_{\mathrm{jsr}} = \sum_{i=1}^{N_c} \frac{\Theta(R^i_{\mathrm{jsr}} - |\mathbf{r} - \mathbf{r}_i|) I_{\mathrm{refill},i}}{\frac{4}{3}\pi \left(R^i_{\mathrm{jsr}}\right)^3}. \tag{S9}$$

$I_{\mathrm{refill,i}}$ denotes the current from the network SR to the ith jSR. The radius of the sink volume in the lumen of the SR is R^i_{jsr}. This flux and a stationary buffer contribute to SR Ca^{2+} concentration dynamics

$$\frac{\partial c_{\mathrm{sr}}}{\partial t} = \nabla \cdot (\mathbf{D}_{\mathrm{sr}} \nabla c_{\mathrm{sr}}) - J_{\mathrm{jsr}} + \frac{\nu_{\mathrm{sr}}}{\nu_{cyt}} (J_{\mathrm{pump}} - J_{\mathrm{leak}}) \text{ in } \Omega \times [0, T]. \tag{S10}$$

$\mathbf{D}_{\mathrm{sr}}$ is the diffusion coefficient for the SR Ca^{2+} concentration. The bi-domain approximation for cytosol and SR is used [12]. In this concept both compartments occupy the same volume continuously with volume ratio $\nu_{\mathrm{sr}}/\nu_{\mathrm{cyt}}$. A zero-flux Neumann boundary condition for the SR Ca^{2+} is imposed on the domain boundary.

The RyR state transitions are determined according to a fixed closing rate, k_{close}, and an opening rate given by

$$k_{\mathrm{open}} = k_{\mathrm{plus}} \phi c^{\eta}_{\mathrm{di}}, \text{ with } \phi = \phi_b + \left(\frac{c_{\mathrm{jsr}}}{\phi_k}\right)^4. \tag{S11}$$

The number of RyRs N^i_{RyR} in the ith CRU is drawn from the distribution $P(N)$

$$P(N) = \begin{cases} \frac{1}{N_N} e^{-\frac{N}{N_{\mathrm{RyR}}}}, & 8 \le N \le 80 \\ 0, & \text{otherwise} \end{cases}. \tag{S12}$$

N_N normalizes the distribution. The upper cutoff was chosen because the size distribution measured in ref [11] has well declined at this value and channel numbers larger than 80 lead in combination with the placement algorithm to large CRUs, larger than a typical CRU-CRU-distance.

We use previously developed CRU model [16], which has a spatially resolved description of the dyadic cleft channel placement and representation of the jSR. The dyadic cleft is assumed to be a cylinder with a height of 15 nm, where the RyRs at the jSR membrane are co-localized to the LCCs at the T-tubule membrane. The behaviour of the CRU is mainly governed by three different dynamics: the gating of the main Ca^{2+} -channels (LCCs and RyRs), the Ca^{2+}-profile within the dyadic cleft and the Ca^{2+}-dynamics of the jSR.

The Ca^{2+} concentration in the cleft (c_{di}) is modeled by a partial differential equation in cylindrical coordinates [4, 15, 16, 19]

$$\frac{\partial c_{\mathrm{di}}}{\partial t} = \sum_{k=1}^{N^i_{\mathrm{LCC}}} I^k_{\mathrm{LCC}} \delta(\mathbf{r} - \mathbf{r_k}) + \sum_{k=1}^{N^i_{\mathrm{RyR}}} I^k_{\mathrm{RyR}} \delta(\mathbf{r} - \mathbf{r_k}) + D_c \Delta_{r,\varphi} c_{\mathrm{di}}(\mathbf{r}) - \frac{\partial}{\partial z} J_z. \tag{S13}$$

The electro-diffusive flux resulting from membrane surface charges is J_z and takes the buffering effect of membranes into account.

The Ca^{2+} concentration is computed from a quasi-steady state approximation for this equation. It is quasi-steady since changes of the jSR-concentration affecting RyR currents and the boundary conditions at the rim of the cleft are taken into account [4]. The stationary solution for given boundary conditions and jSR concentration is

$$c_{\mathrm{di}}(\mathbf{r}) = Z(z_i)c_{\mathrm{bulk}} + \sum_{k=1}^{N^i_{\mathrm{LCC}}} I^k_{\mathrm{LCC}}\eta(\mathbf{r}_k,\mathbf{r}) + \sum_{j=1}^{N^i_{\mathrm{RyR}}} I^j_{\mathrm{RyR}}\eta(\mathbf{r}_j,\mathbf{r}). \tag{S14}$$

with

$$\eta(\mathbf{r}_i,\mathbf{r}) = \frac{Z(z)}{\beta_d h^* D_c} G((r,\phi),(\rho_i,\phi_i)), \tag{S15}$$

where $Z(z) = \exp(-2\phi_0 \exp(-\kappa z))$ describes the gradient resulting from electrodiffusion [4, 15, 16, 19], $h^* = \int_0^h dz Z(z)$ and β_d is a constant buffering factor. The boundary conditions are determined by the bulk Ca^{2+} concentration averaged over the boundary of the dyadic space. $G((r,\phi),(\rho_i,\phi_i))$ is Green's function. Since the RyR- and LCC-currents depend on the local Ca^{2+} concentration at the channel mouths, we cannot use a superposition of single channel Green's functions but Eq. S14 defines a system of linear algebraic equations realizing the coupling of currents by dyadic diffusion and providing the local concentration values [4, 15, 16, 19].

We do not know any experimental results on the correlation between RyR number and the size of the dyadic space. Hence, we made the assumption that the radius of the dyadic space is such that the RyR cluster determined from the placement model can be accommodated with a minimum distance between any RyR and the cleft boundary of 60 nm.

The RyR-currents are proportional to the concentration difference $c_{\mathrm{jsr,i}} - c_{\mathrm{di}}$ [4, 15, 16, 19]. The concentration of $c_{\mathrm{jsr,i}}$ in the ith jSR obeys an ordinary differential equation [4, 19]:

$$\frac{dc_{\mathrm{jsr,i}}}{dt} = \frac{1}{\beta_{\mathrm{jsr}}\nu_{\mathrm{jsr,i}}}\left(I_{\mathrm{refill}} - \sum_{j=1}^{N^i_{\mathrm{RyR}}} I^j_{\mathrm{RyR}}\right) \tag{S16}$$

$$I_{\mathrm{refill}} = \frac{S(\mathbf{r_i}) - c_{\mathrm{jsr,i}}}{\tau_{\mathrm{refill}}}\nu_{\mathrm{jsr,i}} \tag{S17}$$

$$\beta_{\mathrm{jsr}} = 1 + \frac{nK_{\mathrm{csqn}}B_{\mathrm{csqn}}}{(K_{\mathrm{csqn}} + c_{\mathrm{jsr,i}})^2}. \tag{S18}$$

Details are explained in ref. [4]. I_{refill} is the diffusive current from the network SR. The factor β_{jsr} describes buffering by Calsequestrin.

The electrophysiology is based on Mahajan et al. [14] and was adapted to the above CRU modelling concept. The dynamics of the membrane potential V_m is given by:

$$\frac{dV_m}{dt} = -(I_{\mathrm{ion}} + I_{\mathrm{stim}}). \tag{S19}$$

Here, I_{stim} is the current to depolarize the cell. The ion current is given by

$$I_{\mathrm{Ion}} = I_{\mathrm{Na}} + I_{\mathrm{to,f}} + I_{\mathrm{to,s}} + I_{\mathrm{Kr}} + I_{\mathrm{Ks}} + I_{\mathrm{K1}} + I_{\mathrm{NaK}} + I_{\mathrm{CaL}} + I_{\mathrm{NCX}}, \tag{S20}$$

where I_{Na} is the fast Na^+ current, $I_{\mathrm{to,f}}$ is the fast and $I_{\mathrm{to,s}}$ the slow component of the rapid outward K^+ current, I_{Kr} is the rapid delayed rectifier current, I_{Ks} is the slow delayed rectifier current, I_{K1} is the inward rectifier current, and I_{NaK} is the Na^+/K^+-pump current.

The LCC current is denoted by I_{CaL} (mV/ms), which is the sum of all LC channel currents over all CRUs in the model. The NCX current I_{NCX} (mV/ms), is the integral of the local flux J_{NCX} over the simulation domain and its boundary.

Numerical methods

Due to the presence of multiple scales in space and time, the stochasticity of CRU behaviour and the coupling of partial differential equations (PDEs) for concentrations and ordinary differential equations (ODEs) for the membrane potential the model exhibits some challenges with respect to numerical methods. Therefore, we dedicated previous studies to develop numerical methods living up to these requirements [19, 4]. In particular the recent study [4] published in the applied mathematics journal SIAM Multiscale Modelling & Simulations describes the methods used in this study and explains and motivates all the numerical methods in detail. Here, we provide a short overview only.

For the vast majority of complex geometries and model problems, the PDEs cannot be solved with analytical methods. Instead, an approximation of the equations can be constructed, typically based upon different types of numerical methods. We use the Finite Element Method (FEM), which is arguably the most powerful method known for the numerical solution of boundary- and initial-value problems characterized by partial differential equations. The spatial discretization of the given PDEs by the finite element method leads to a system of ODEs for transient problems. To solve such ODEs, we use an adaptive higher order Runge-Kutta time-stepping scheme, specifically the ROWDA3 [13] method. At each time step of the ROWDA3 method, the discretized model equations lead to a set of algebraic equations which are solved by a biconjugate gradient stabilized method (BiCGSTAB) [18] with ILU preconditioner.

We use the forward Euler method for the membrane potential dynamics and Rush-Larsen time step integrator for the gating and concentration equations. Our numerical schemes are implemented in C++ and were developed based on the public domain FEM package DUNE [1] and Dune-PDELab [2], which allows for highly parallelized computations. Computations were performed on the high performance compute cluster at the Max Delbrück Center for Molecular Medicine in Berlin as well as at the Max Planck Institute for Dynamics and Self-Organization in Göttingen. AP simulations were performed on 4 InfiniBand or OmniPath nodes with 16 cores each, where each simulation takes about 30 h to simulate 15 APs. Spark simulations were performed on 8 InfiniBand or OmniPath nodes, where each simulation took about 36 h.

Error estimates for polynomial chaos expansion

The least-square fit error determines the regression error of the whole data set, the cross-validation error describes over-fitting by splitting the data set into training- and test-data. Here we used a k-fold method with (k=10) for cross validation [10]. Let $\mathcal{I}$ be an index subset of $\{1, \ldots, N\}$, where N is number of data points. The R^2-score is defined as

$$R^2 = 1 - \frac{\sum_{i\in\mathcal{I}}(Y_i - \hat{Y}_i)^2}{\sum_{i\in\mathcal{I}}(Y_i - \bar{Y})^2}. \tag{S21}$$

Here, Y_i denotes the actual biomarker output from the simulations, $\hat{Y}_i$ the value from the polynomial regression and $\bar{Y}$ is the mean value of the data points in the data set. The coefficient of determination is calculated from the R^2-score for the whole data set, meaning $\mathcal{I} \equiv \{1, \ldots, N\}$. In case of the cross-validation coefficient, we calculated the average of the R^2-score from the test-sets, which arises from the splitting of the data-set by the k-fold method.

We furthermore penalized the number of coefficients by employing the commonly used LASSO (least absolute shrinkage and selection operator) method using a python library for machine learning called `scikit-learn` We determined the polynomial degree as well as the penalty parameter for the lasso method, which result in minimal cross-validation error for each biomarker. In Figure S2, the coefficient of determination, cross-validation coefficient and the mean absolute percentage error (MAPE) are shown for APD_{90}. The MAPE is defined as

$$\text{MAPE} = \frac{100\%}{n}\sum_{i=1}^{n}\left|\frac{Y_i - \hat{Y}_i}{Y_i}\right|. \tag{S22}$$

Note the MAPE comprises uncertainty in the model output and regression error. Since the model is stochastic, the output cannot be predicted with absolute certainty and, therefore, the MAPE is not converging to zero even if the mean is described well by the polynomial regression.

References

[1] P. Bastian, M. Blatt, A. Dedner, C. Engwer, R. Klöfkorn, R. Kornhuber, M. Ohlberger, and O. Sander. A generic grid interface for parallel and adaptive scientific computing. Part II: implementation and tests in DUNE. *Computing*, 82(2):121–138, 2008.

[2] P. Bastian, F. Heimann, and S. Marnach. Generic implementation of finite element methods in the distributed and unified numerics environment (DUNE). *Kybernetika*, 46(2):294–315, 2010.

[3] Marco Bertamini, Michele Zito, Nicholas E. Scott-Samuel, and Johan Hulleman. Spatial clustering and its effect on perceived clustering, numerosity, and dispersion. *Attention, Perception, & Psychophysics*, 78(5):1460–1471, Jul 2016.

[4] N. Chamakuri, W. Neubert, S. Gilbert, J. Vierheller, G. Warnecke, and M. Falcke. Multiscale modeling and numerical simulation of calcium cycling in cardiac myocytes. *SIAM Multiscale Modeling & Simulation*, 16(3):1115–1145, 2018.

[5] Heping Cheng and WJ Lederer. Calcium sparks. *Physiological Reviews*, 88(4):1491–1545, 2008.

[6] D Fedida and WR Giles. Regional variations in action potentials and transient outward current in myocytes isolated from rabbit left ventricle. *The Journal of Physiology*, 442(1):191–209, 1991.

[7] Philip Gemmell, Kevin Burrage, Blanca Rodríguez, and T Alexander Quinn. Rabbit-specific computational modelling of ventricular cell electrophysiology: Using populations of models to explore variability in the response to ischemia. *Progress in Biophysics and Molecular Biology*, 121(2):169–184, 2016.

[8] Joshua I Goldhaber, Scott T Lamp, Donald O Walter, Alan Garfinkel, Gary H Fukumoto, and James N Weiss. Local regulation of the threshold for calcium sparks in rat ventricular myocytes: role of sodium-calcium exchange. *The Journal of physiology*, 520(2):431–438, 1999.

[9] David A Golod, Rajiv Kumar, and Ronald W Joyner. Determinants of action potential initiation in isolated rabbit atrial and ventricular myocytes. *American Journal of Physiology-Heart and Circulatory Physiology*, 274(6):H1902–H1913, 1998.

[10] Trevor Hastie, Robert Tibshirani, and Jerome Friedman. *The elements of statistical learning: data mining, inference, and prediction, Springer Series in Statistics*. Springer New York, 2009.

[11] Isuru Jayasinghe, Alexander H. Clowsley, Ruisheng Lin, Tobias Lutz, Carl Harrison, Ellen Green, David Baddeley, Lorenzo Di Michele, and Christian Soeller. True molecular scale visualization of variable clustering properties of ryanodine receptors. *Cell Reports*, 22(2):557 – 567, 2018.

[12] James P Keener and James Sneyd. *Mathematical physiology I: Cellular Physiology*. Springer, 2nd ed., 2009.

[13] J. Lang. *Adaptive Multilevel Solution of Nonlinear Parabolic PDE Systems*, volume 16 of *Lecture Notes in Computational Science and Engineering*. Springer-Verlag, Berlin, 2001.

[14] Aman Mahajan, Yohannes Shiferaw, Daisuke Sato, Ali Baher, Riccardo Olcese, Lai-Hua Xie, Ming-Jim Yang, Peng-Sheng Chen, Juan G Restrepo, Alain Karma, et al. A rabbit ventricular action potential model replicating cardiac dynamics at rapid heart rates. *Biophysical Journal*, 94(2):392–410, 2008.

[15] Thomas Schendel and Martin Falcke. Efficient and detailed model of the local Ca^{2+} release unit in the ventricular cardiac myocyte. *Genome Informatics*, 22:142–155, 2009.

[16] Thomas Schendel, Rüdiger Thul, James Sneyd, and Martin Falcke. How does the ryanodine receptor in the ventricular myocyte wake up: by a single or by multiple open l-type Ca^{2+} channels? *European Biophysics Journal*, 41(1):27–39, 2012.

[17] Yohannes Shiferaw. Nonlinear onset of calcium wave propagation in cardiac cells. *Physical Review E*, 94(3):032405, 2016.

[18] H. A. van der Vorst. Bi-CGSTAB: A fast and smoothly converging variant of bi-cg for the solution of nonsymmetric linear systems. *SIAM J. Sci. Stat. Comput.*, 13:631–644, 1992.

[19] Janine Vierheller, Wilhelm Neubert, Martin Falcke, Stephen Henry Gilbert, and Nagaiah Chamakuri. A multiscale computational model of spatially resolved calcium cycling in cardiac myocytes: from detailed cleft dynamics to the whole cell concentration profiles. *Frontiers in Physiology*, 6:255, 2015.

[20] Mark A Walker, George SB Williams, Tobias Kohl, Stephan E Lehnart, M Saleet Jafri, Joseph L Greenstein, WJ Lederer, and Raimond L Winslow. Superresolution modeling of calcium release in the heart. *Biophysical Journal*, 107(12):3018–3029, 2014.

2 Supplementary Tables

Table S1: Literature biomarker ranges for Ca^{2+} transients and action potentials. Note that for the values from [9], the standard deviation was calculated from the standard error by $\sigma = \sqrt{n}\hat{\sigma}$. See also Fig. S6.

	target values (literature)	description
Biomarker (AP)		
max V_m	46 ± 4.5 mV [9]	maximal value of action potential peaks
resting V_m	-82.7 ± 1.4 mv [9], ≈ $-85mV$ [14], -81.3 ± 3.9 mV [6]	resting value of the action potential
amplitude (V_m)	127 ± 2.0 mV [9]	difference of resting potential and max V_m
amplitude (dome)	96.5 ± 9.3 mV [6]	difference of resting potential and dome V_m
dome V_m	15.2 ± 10.1 mV [6]	peak in the plateau phase
dV_m/dt	395 ± 47 V/s [9]	maximum rate of rise of the action potential
APD_{50}	104 ms - 117 ms (at 400 ms PCL) [7]	action potential duration at 50%
APD_{90}	142 ms - 188 ms (at 400 ms PCL) [7]	action potential duration at 90%
systolic $[Ca^{2+}]$	0.8 µM - 1.5 µM (at 400 ms PCL)	peak systolic calcium
diastolic $[Ca^{2+}]$	0.15 µM - 0.3 µM (at 400 ms PCL)	diastolic calcium
$[Na^{+}]_i$	10.5 mM - 11.5 mM (at 350 ms PCL) [14]	intracellular sodium
Biomarker (Spark)		
FDHM	8.4 ± 0.5 ms [8] ,≈ 15 ms [17], ≈ 30 ms [5]	full duration at half maximum of a spark
peak $[Ca^{2+}]_i^{exp}$	≈ 1 µM [5]	peak of experimental Ca^{2+} concentration inferred from fluo4 during a spark
peak $[Ca^{2+}]_i$	≈ 10 µM [20]	underlying local peak Ca^{2+} concentration
spark rate	1 $s^{-1}\mu m^{-1}$ [5]	number of spark per section cell (in µm, longitudinal direction) and time (in seconds)

Table S2: Dyadic cleft parameters.

Parameter	Meaning	Value
N_{RyR}	distribution parameter for RyRs per dyadic cleft	20
N_{LCC}	average number of LCCs per dyadic cleft	4
$r_{\mathrm{RyR,LCC}}$	ratio of RyRs and LCCs	5
k_{plus}	rate constant determining the RyR opening rate	varies
k_{close}	closing rate (RyRs)	varies
ϕ_k	$[Ca^{2+}]_{jsr}$- dependent regulation affinity	1.59 mM
ϕ_b	$[Ca^{2+}]_{jsr}$- dependent regulation minimum	0.8025
η	c_{di} sensitivity Hill Coefficient	2.1
μ_{RyR}	step length distribution parameter for average of RyR placement	40.1 nm
σ_{RyR}	step length distribution parameter for standard deviation of RyR placement	7.4 nm
r_{min}	minimum distance for placement	30 nm
r_{chb}	minimum RyR distance to cleft boundary	60 nm
g_{RyR}	RyR permeability	varies

Table S3: Exchanger and uptake parameters.

Parameter	Meaning	Value
g_{NaCa}	strength of Na^+/Ca^{2+}-exchanger	1.8 µM s^{-1}
$f_{\mathrm{NaCa,high}}$	maximal factor for g_{NaCa} at dyadic cleft centers	72.0
$f_{\mathrm{NaCa,low}}$	minimal factor for g_{NaCa} distant to dyadic clefts	0.66
$f_{\mathrm{NaCa,surf}}$	minimal factor for g_{NaCa} at cell surface	0.5
$V_{\mathrm{P,max}}$	maximal rate of SERCA uptake	varies
K_{P}	SERCA uptake threshold	0.4 µM
k_{sat}	constant	0.2
ξ	constant	0.35
$K_{\mathrm{m,Nai}}$	constant	12.3 mM
$K_{\mathrm{m,Na0}}$	constant	87.5 mM
$K_{\mathrm{m,Cai}}$	constant	3.6×10^{-3}
$K_{\mathrm{m,Cao}}$	constant	1.3 mM
c_{naca}	constant	0.3 µM

Table S4: Constants involved in computing transition rates for LCC channels.

Parameter	Meaning	Value
s_1'	voltage-inactivation rate	0.00195 ms^{-1}
r_2	closing rate	3.0 ms^{-1}
k_p^0	half-rate Ca^{2+} binding constant	180.0 μM
τ_{po}	average closed time	1.0 ms
r_1	uninhibited open rate	0.3 ms
k_1'	voltage-inhibition rate	0.00413 ms^{-1}
T_{Ba}	fitting parameter	450.0 ms
k_2	Ca^{2+} unbinding rate (LCCs)	1.03615×10^{-4} ms^{-1}
k_2'	voltage-Inhibition resolution rate	2.24×10^{-4} ms^{-1}
$\bar{c_p}$	half-rate constant for deep Ca^{2+} inhibition	60.0 μM
g_{LCC}	LCC permeability	varies

Table S5: Constants relevant to diffusion model inside the dyadic space.

Parameter	Meaning	Value
ϕ_0	dimensionless constant	-2.2
κ	inverse of the Debye length	1 nm^{-1}
D_c	diffusion constant for Ca^{2+} in the dyadic space	0.1 $\mu m^2 ms^{-1}$
h	height of the dyadic space cylinder	15 nm
R	radius of the dyadic space cylinder	varies
R_B	universal gas constant	8.31 $kJ(K\ mol)^{-1}$
T	temperature of the cell	308 K
β_d	buffering factor	2

Table S6: Constants and parameters involved in modelling the Ca^{2+} dynamics in the jSR.

Parameter	Meaning	Value
B_{csqn}	total calsequestrin concentration	800 μM
n	number of calsequestrin binding sites	15
K_{csqn}	dissociation constant of calsequestrin	600 μM
ν_{jSR}	volume of the jSR	varies
τ_{refill}	refill flux time constant	0.5 ms

Table S7: Buffering and diffusion parameters.

Parameter	Description	Value
b_m^{tot}	total concentration of calmodulin (mobile buffer)	25.0 µM
b_s^{tot}	total concentration of troponin C (stationary buffer)	70.0 µM
B_{sr}^{tot}	total concentration of jSR buffer	1500.0 µM
b_{Fluo-4}^{tot}	total concentration of Fluo-4	25.0 µM
D_c	diffusion constant of cytosolic Ca^{2+}	0.22 $\frac{\mu m^2}{ms}$
D_{b_m}	diffusion constant of calmodulin	0.04 $\frac{\mu m^2}{ms}$
D_{b_s}	diffusion constant of troponin C	0 $\frac{\mu m^2}{ms}$
D_{b_f}	diffusion constant of Fluo-4	0.033 $\frac{\mu m^2}{ms}$
D_S	diffusion constant of sarcoplasmic Ca^{2+}	0.2 $\frac{\mu m^2}{ms}$
k_s^+	on rate for troponin C binding	0.043 μM^{-1} ms^{-1}
k_s^-	off rate for troponin C binding	0.026 ms^{-1}
k_m^+	on rate for calmodulin binding	0.023 μM^{-1} ms^{-1}
k_m^-	off rate for calmodulin binding	0.238 ms^{-1}
ν_{sr}/ν_{cell}	ratio of SR to cell volume	0.08
ν_{jsr}/ν_{cell}	ratio of jSR to cell volume	0.005
ν_{cyt}/ν_{cell}	ratio of cytosolic volume to cell volume	0.915

Table S8: Initial Values.

Parameter	Description	Value
c	free cytoplasmic Ca^{2+} concentration	0.1 µM
b_x	buffered cytosolic Ca^{2+} (for $x = m, s, f$)	$\frac{b_x^{tot} \cdot c}{k_x^+/k_x^- + c}$
S	free sarcoplasmic Ca^{2+} concentration	1200 µM

Table S9: Ionic current conductances.

Parameter	Meaning	Value
g_{Na}	peak I_{Na} conductance	12.0 mS/µmF
$g_{to,f}$	peak $I_{to,f}$ conductance	0.11 mS/µmF
$g_{to,s}$	peak $I_{to,s}$ conductance	0.04 mS/µmF
g_{K1}	peak I_{K1} conductance	0.3 mS/µmF
g_{Kr}	peak I_{Kr} conductance	0.0125 mS/µmF
g_{Ks}	peak I_{Ks} conductance	0.1386 mS/µmF
g_{NaK}	peak I_{Kr} conductance	1.5 mS/µmF

3 Supplementary Figures

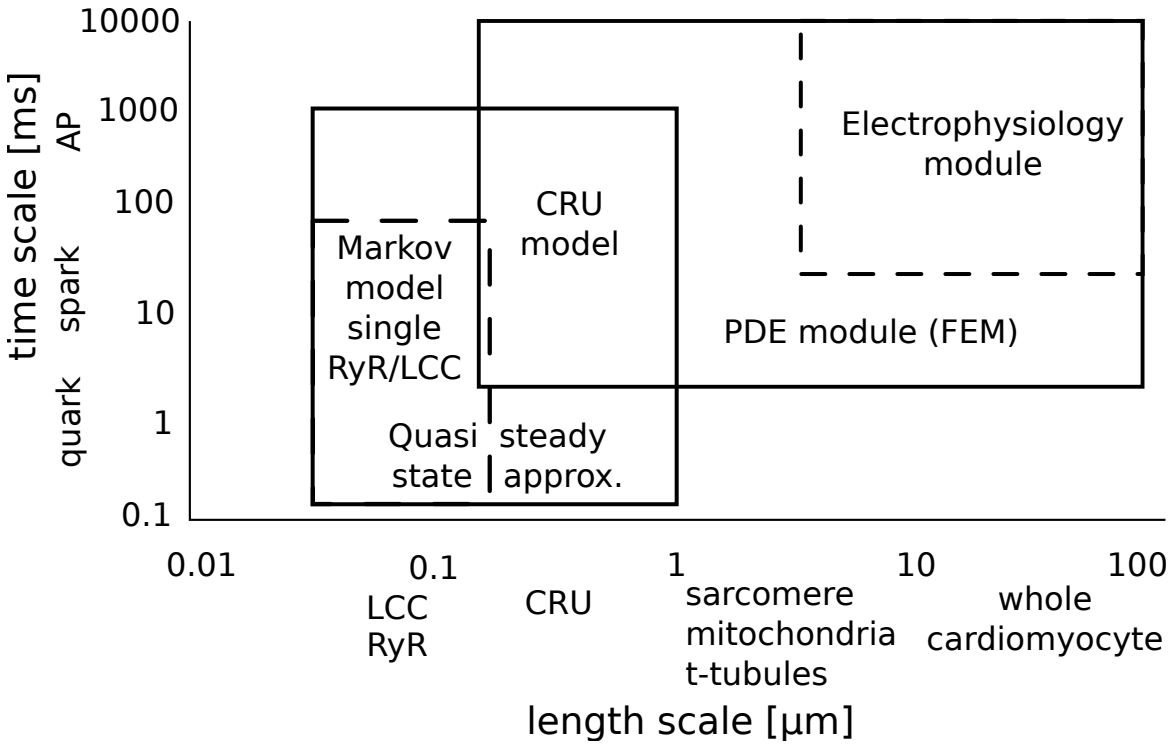

Figure S1: The mathematical model covers several spatial and temporal scales. On the shortest length and time scales a quasi-steady state approximation for the dyadic concentration profiles and a Markov model for the individual channels is employed to model Ca^{2+} dynamics on the spatial and temporal scales in the dyadic cleft. The PDE module links the whole cell electrophysiology to the signalling in the local CRU micro-domain.

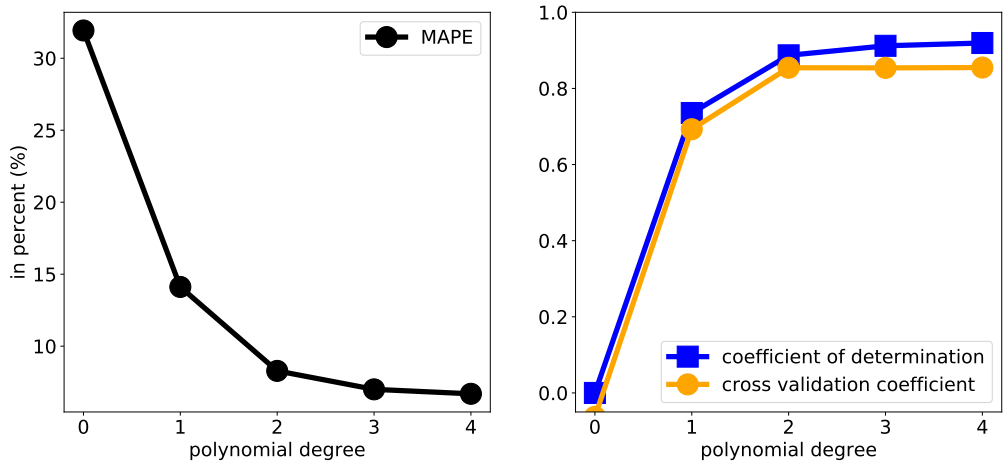

Figure S2: The mean absolute percentage error (MAPE), the coefficient of determination and the cross validation error for the example of the systolic peak Ca^{2+} biomarker.

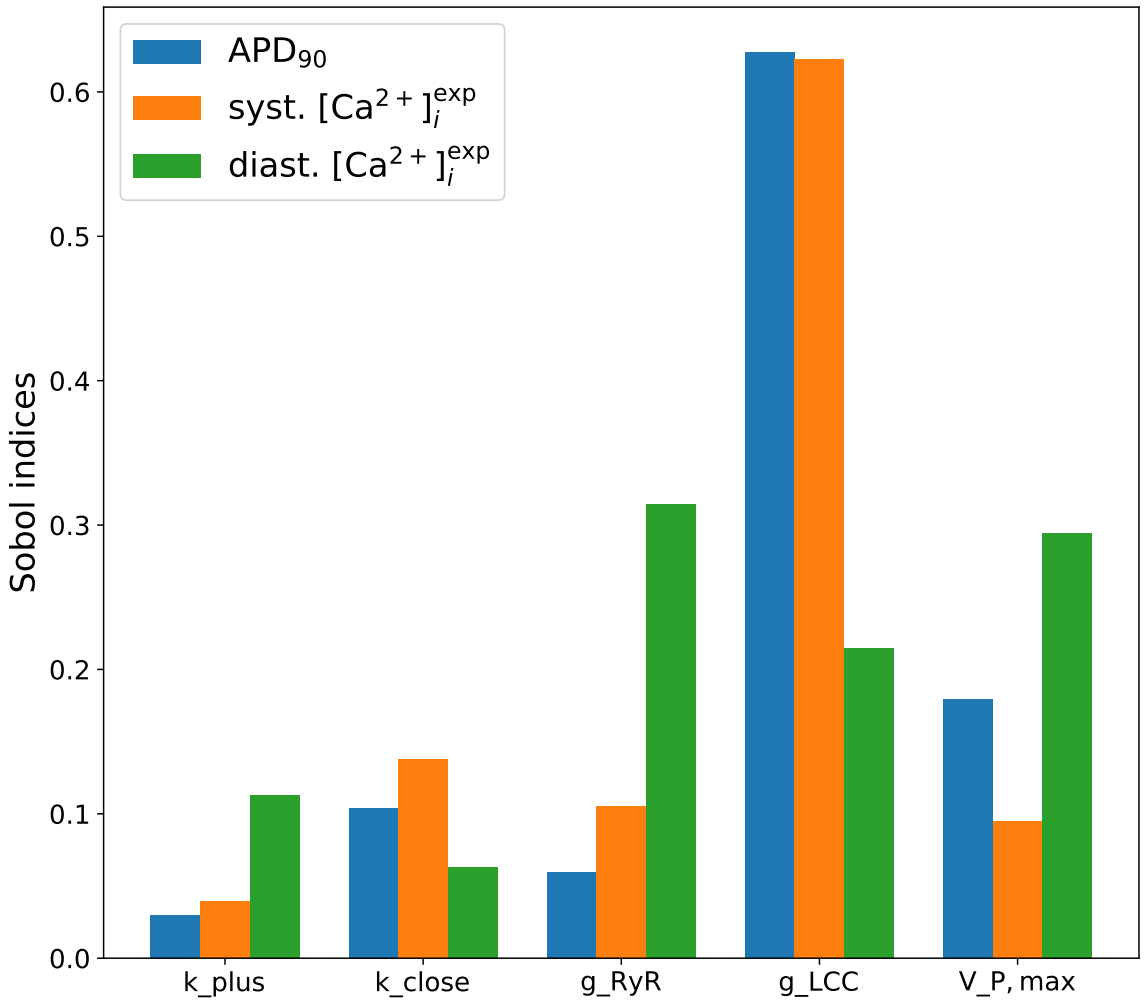

Figure S3: Calculation of Sobol indices as a measure for global sensitivities for action potential biomarkers.

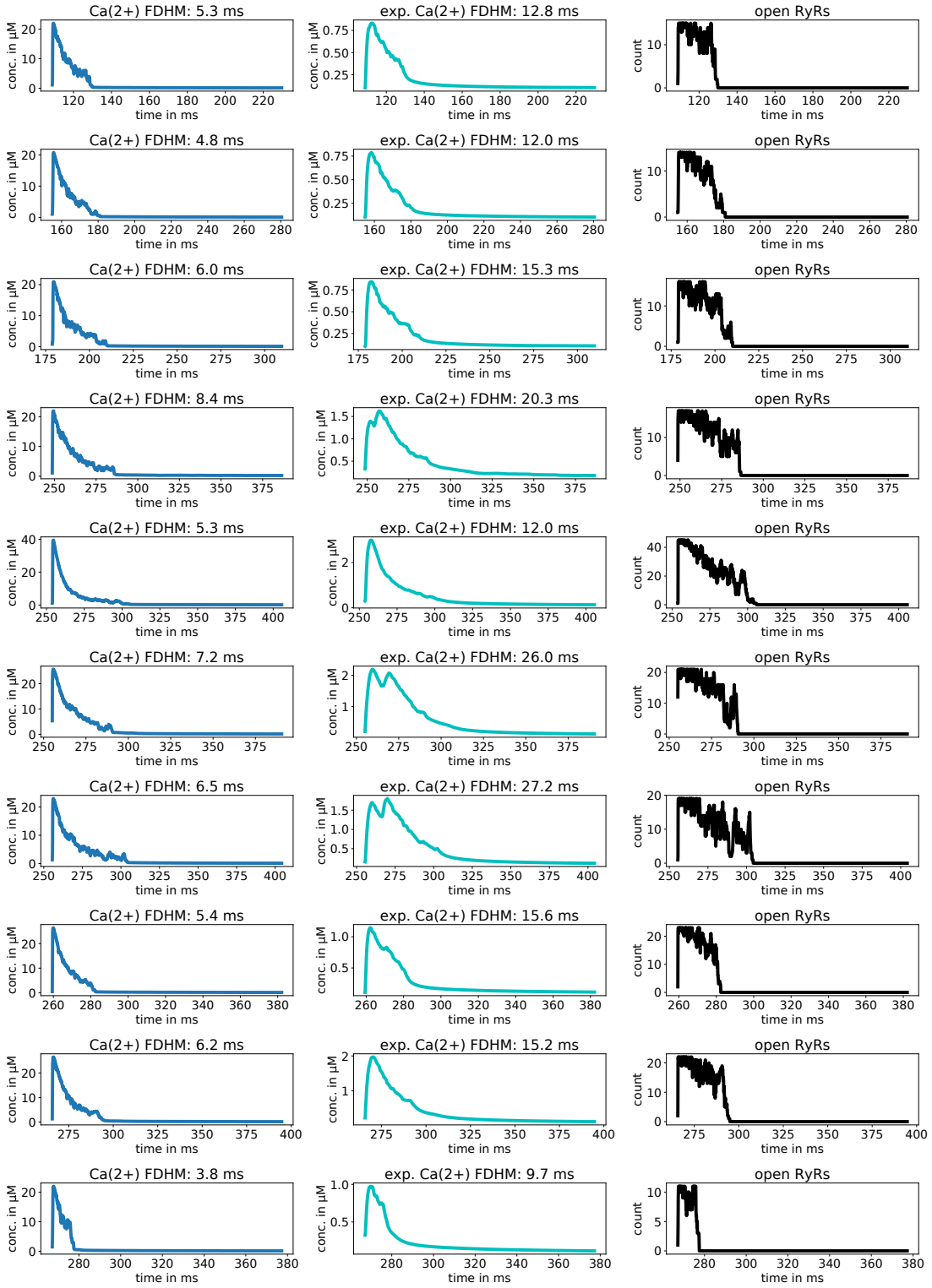

Figure S4: Comparison of experimental Ca^{2+} inferred from the buffer and the underlying simulated Ca^{2+}.

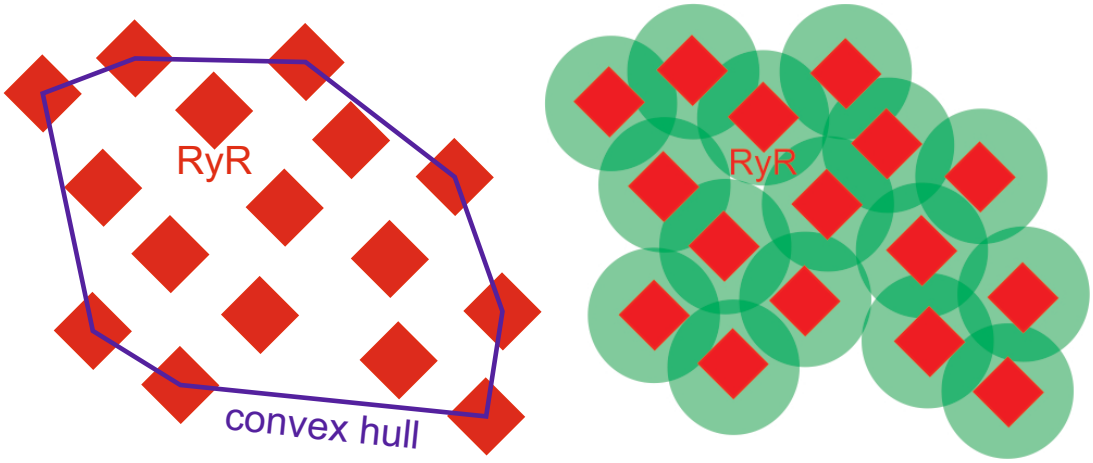

Figure S5: Left panel: We determine the area per channel using the concept of convex hull [3]. The hull wraps around the channels of a cluster like a police line around a group of tress does. The line goes through the center point of channels. The area per channel is determined as the area inside the convex hull divided by the number of channels. Note, channels on the hull contribute less to the area than inner channels. Hence, the channel per area is smaller than the square of the channel distance in a regular quadratic configuration of channels. Specifically we used https://docs.scipy.org/doc/scipy/reference/generated/scipy.spatial.ConvexHull.html. Right panel: A circular area of influence (green) is appointed to each channel. We denote the sum of the areas of influence of all channels with Σ and the sum of all overlap areas with Ω. The mean occupancy is defined as 1-Ω/Σ [3]. Mean occupancy is small, if channels are close to each other and the overlap is large. The regular placement has smaller mean occupancy (≈ 0.36) than the placement according to Jayasinghe et al. (mean occupancy ≈ 0.49) with measured parameters from [11].

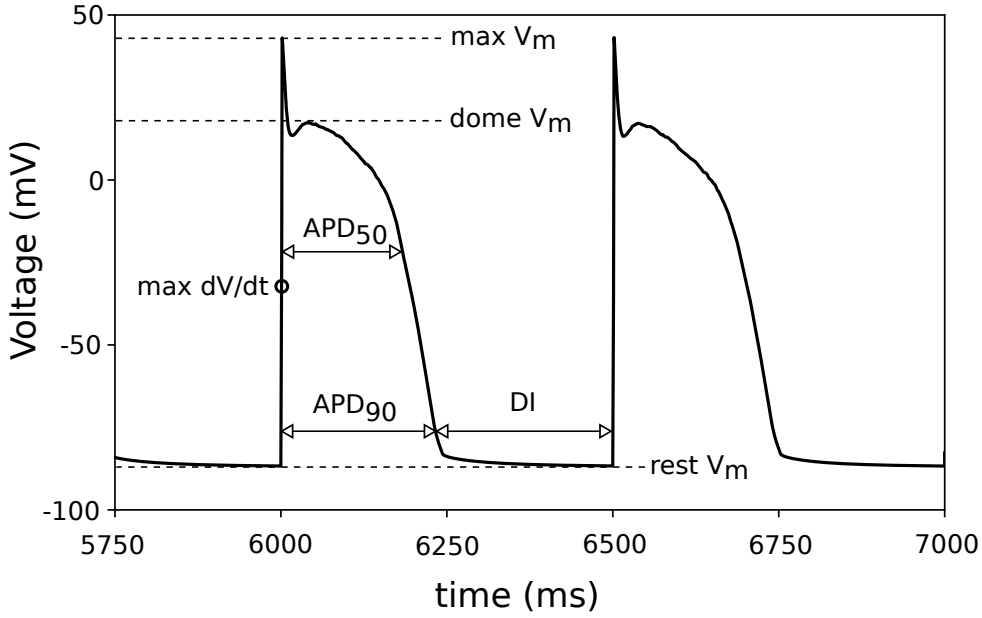

Figure S6: Action potential (AP) characterization.

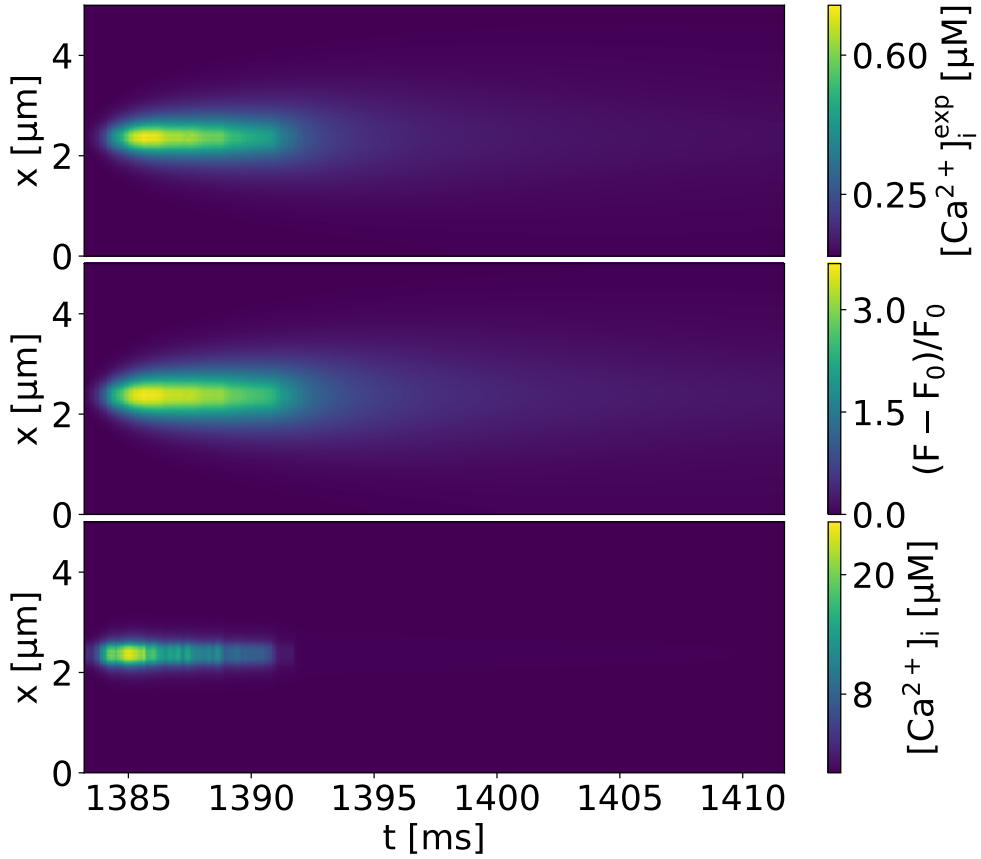

Figure S7: Example linescans of a spark in a 2.5 µm surrounding of a CRU. Shown are the concentrations of Fluo-4 bound Ca^{2+} and cytosolic Ca^{2+} in the upper and lower panel respectively and the values of $\Delta F/F_0$ in the center one. The considered cleft has a total number of 10 RyRs, a radius of 185.9 nm and the spark a FDHM of 7.2 ms.